Microstructure and corrosion resistance of ultrahigh pressure Mg-8Li based alloys.

YANG, M., FENG, J., HU, H., NIU, T., GAO, W., ZOU, G., FERNANDEZ, C., REN, L. and PENG, Q.

2023

Microstructure and Corrosion Resistance of Ultrahigh Pressure Mg-8Li Based alloys

Meng Yang[1], Jiawen Feng[1], Haidong Hu[1], Tingting Niu[1], Wei Gao[1], Guodong Zou [1], Carlos Fernandez[2], Liqun Ren[3], Qiuming Peng [1,]*

[1]State Key Laboratory of Metastable Materials Science and Technology, Yanshan University, Qinhuangdao 066004, P.R. China

[2]School of Pharmacy and Life Sciences, Robert Gordon University, Aberdeen AB107GJ, U.K.

[3]Laboratory of Spinal Cord Injury and Rehabilitation, Chengde Medical University, Chengde 067000, China.

Abstract

High anti-corrosion Mg alloys is desirable to expand their industrial applications. Herein we report an outstanding corrosion resistance of dual-phase Mg-8Li-Y alloy using ultrahigh pressure (UHP) technology. The average corrosion rate is ~0.47 mm/y, overwhelming the majority of Mg-Li alloys reported hitherto. *In-situ* X-ray diffraction and scanning electron microscope observation demonstrate that a unique multiple-film on UHPed Mg-8Li-Y alloy attributes to the excellent corrosion resistance, which origins from the dynamic dissolution/regeneration of Li_2CO_3-rich composite film, thus effectively prohibiting corrosion solution permeation. These results provide some implications to design good anti-corrosion coating for Mg, ever stainless Mg alloys.

Keywords: Mg-Li alloys; Ultrahigh pressure; Surface films; Corrosion properties

Email address: pengqiuming@ysu.edu.cn.

1 Introduction

Lightweight is the most prominent feature of magnesium (Mg) alloys, whereas its weak formability at low temperatures and poor corrosion resistance severely prohibit their widespread applications [1-4]. Therefore, how to achieve high plasticity Mg alloys together with good corrosion properties become an important issue in the fields of Mg alloys [5]. Alloying lithium (Li) element paves a potential way to solve this problem because the *c*/*a* axial ratio has been reduced for Mg-Li alloys, thus featuring better formability in contrast to other Mg-based alloys [6]. According to the Mg-Li binary phase diagram, the Li content affects crystal structure of Mg-Li alloys. Especially, Mg-Li alloys containing 5.5-10.3 wt.% Li exhibit a dual-phase structure, *i.e.*α-Mg (HCP) and β-Li (BCC) phases. Differing from hard the α-Mg phase, the β-Li phase with BCC structure has good ductility and machinability compared with the hard α-Mg phase. Hence, dual-phase Mg-Li alloys generally present better combinations of strength, elongation, and superplasticity than single-phase alloys (α-Mg or β-Li), and are potentially attractive in a variety of applications [7-10].

Unfortunately, as extremely active metallic elements, Mg and Li are prone to corrosion reactions in humid air. β-Li is more reactive than α-Mg matrix and is more sensitive to local corrosion at the α-Mg/β-Li interface [11]. Additionally, the α-Mg matrix contains some Li atoms with higher activity. Thus, the corrosion resistance of dual-phase Mg-Li alloys is normally poorer than that of Mg alloys without Li. The corrosion products on the surface of Mg-Li alloys include magnesium hydroxide ($Mg(OH)_2$), magnesium oxide (MgO), magnesium carbonate ($MgCO_3$), lithium oxide (Li_2O), lithium hydroxide (LiOH) and lithium carbonate (Li_2CO_3) [4, 12]. Normally, the surface oxide film composed of MgO and $Mg(OH)_2$ is loose, which shows limited protection on the Mg matrix under corrosion conditions. The Li element dissolves from the film during the corrosion process, and the residual surface layer is gradually fluffy, which accelerates the corrosion of the alloy, and results in a higher risk of corrosion failure in the service of Mg-Li alloy components [13].

Basically, differing from other Mg alloys, the oxide film characters of Mg-Li alloys are complex, and sensitive to environment. Xu *et al* [14] have conducted the detailed electrochemical analysis and physical measurement of Mg-14 wt.% Li based

alloys, aiming to understand the corrosion mechanism of the surface oxide film on Mg-Li alloys and solve the passivation. The excellent corrosion resistance of Mg-Li alloys with body-centered cubic structure attributes to a combination of many factors, including [12] the uniform nanoscale microstructure through designing alloy composition and processing; and the protective lithium carbonate film with a surface covering area, which is much larger than the traditional closely packed Mg-based alloys. The uniform Li_2CO_3 film is able to resist the environmental corrosion and regenerate naturally when the alloy surface is damaged [3]. In this regard, the development of Li_2CO_3 coating or Li_2CO_3 composite shed light on the high performance of Mg alloys.

More recently, our group developed a high specific strength of Mg-Li alloy *via* a strategy of coherent interfaces strengthening using an industrial ultrahigh pressure (UHP) technique [15]. Analogous to grain refining and precipitation strengthening, the distinctive structures remarkably achieve a high microhardness (108~120 HV) and a specific yield strength (160~182 $kNmKg^{-1}$), companying with a good ductility (20~24%) at room temperature [16]. Herein, we attempt to study their corrosion properties and related mechanisms: i) investigate the effect of UHP process on corrosion properties of Mg-Li based alloys; ii) clarify the corrosion process and corrosion mechanism of Li_2CO_3 composite oxide film.

2 Experiment and method

2.1 Sample preparation

Both Mg-8Li (wt.%, all compositions given thereafter in wt.%) and Mg-8Li-1Y alloy ingots were prepared by vacuum-induction melting method under a protective gas of argon. The as-cast alloy was machined into a cylinder with a diameter of 70 mm and a height of 14 mm for ultrahigh pressure (UHP). The pressure was loaded to 6 GPa before the system was heated up. The temperature was raised to 700 °C at a rate of 30 °C/min and remained for 30 min. Then, it was cooled to room temperature naturally before unloading the pressure. Four samples, such as as-cast Mg-8Li (denoted by Mg-8Li-AC), ultrahigh pressure Mg-8Li (denoted by Mg-8Li-UHP-700), as cast Mg-8Li-1Y (denoted by Mg-8Li-Y-AC) and ultrahigh pressure Mg-8Li-1Y (denoted by Mg-8Li-Y-UHP-700), were involved in the experiments.

2.2 Microstructure characteristics

The samples were polished by a sequence of sandpapers. The surface of the sample was etched with a 5% HNO_3 - 95% C_2H_5OH solution for 10-20 s before observation. The phase composition was analyzed by X-ray diffraction (XRD), which was performed by the SmartLab equipment (Rigaku, Japan) with Cu Kα radiation (λ = 1.5406 Å) in a 2θ range from 20° to 60° with a scanning rate of 4 ° min^{-1}. The surface morphology was observed by optical microscopy (OM, ZEISS AXIOVERT 200 MAT). The microstructure characteristics of the samples were identified by focused ion beam scanning electron microscope (FIB-SEM, FEI-Helios G4 CX) with a voltage of 5 kV and a current of 0.14 nA.

2.3 Corrosion behaviors

The corrosion resistance of Mg-Li alloys was investigated by electrochemical tests and hydrogen evolution test. All electrochemical tests were recorded by potentiostat-frequency response analysis system (Bio-logic, VSP), and fitted by the EC-Lab software. The electrochemistry tests were performed by three electrodes, wherein the platinum-mesh electrode was positioned directly facing the working electrode, and the reference electrode (saturated calomel electrode, SCE) was located between the two electrodes and directly against the sample (*i.e.* the working electrode). All tests were performed in 3.5 wt.% sodium chloride (NaCl) solution at room temperature. The open circuit potential (OCP) was assessed for 5 h. The dynamic polarization curves were obtained by scanning potential variation in a range of -2.0 to -1.2 V (*vs*. SCE) with a scanning speed was 0.3 mV/s after immersing in solution for 1 h to obtain a relatively stable OCP. The electrochemical impedance spectroscopy (EIS) was tested with a frequency range of 100 kHz to 0.1 Hz after immersing in solution for 12 h. The corrosion rate of Mg-Li alloys was evaluated by recording the weight change of alloys before and after corrosion together with the hydrogen evolution test. The sample was sealed with epoxy resin, and the exposed metal area was 0.785 cm^2. The test duration was 200 h, and the corrosion products were removed with 20% chromic acid solution. At least three parallel experiments were conducted for each sample to ensure data accuracy and reproducibility.

2.4 *In-situ* observations

In-situ morphology variations of surface film in 3.5 wt.% NaCl solution were monitored and recorded by high definition CCD video microscope (BYH-38MP) in real time. Video record was performed by a continuous magnification monocular microscope with long working distance, wide field of vision and high definition imaging quality. Constant parameters were used before test observation, and then high definition real-time images can be obtained. Specifically, the samples were fixed on the stage, and then the immersion solution was added. The clear samples at a magnification of 0.7X were observed by rotating variable power main objectivity. Vertical light illumination was provided by ring fluorescent lamps. The S-EYE software was used for video recording.

In addition, the different corrosion products were analyzed by near *in-situ* XRD method. Specifically, the same sample was immersed in a 3.5 wt.% NaCl solution for different soaking times with an average interval soaking time of 1 h. Subsequently, the sample was dried at room temperature for 2 min, and then tested immediately to avoid the oxidation in the atmosphere.

Movie 1: *in-situ* immersion observation of Mg-8Li-Y-UHP-700 alloys for 250 h.

Movie 2: Rapid formation/dissolution process of the black oxide film containing Li_2CO_3.

Movie 3: The self-healing process of composite oxide film on the surface of Mg-8Li-Y-UHP-700 alloy.

Movie 4: The accumulation of corrosion products on the surface of Mg-8Li-Y-UHP-700 alloy.

3 Results and discussion

3.1 Microstructure characteristics

XRD patterns of Mg-8Li-AC, Mg-8Li-UHP-700, Mg-8Li-Y-AC, and Mg-8Li-Y-UHP-700 are shown in **Fig. 1a**. All samples are mainly composed of α-Mg (Mg-rich) and β-Li (Li-rich) phases, which is consistent with the Mg-Li binary phase diagram [17]. However, the Mg-8Li-UHP-700 alloy shows a higher intensity of α-Mg phase diffraction peak, but a relatively weaker β-Li peak. Meanwhile, the diffraction peak of

Y_2O_3 is detected in both Mg-8Li-1Y and Mg-8Li-Y-UHP-700 alloys. Besides, differing from the as-cast Mg-8Li-1Y, a new diffraction peak of Li_2CO_3 is detected on Mg-8Li-Y-UHP-700, which means that the Li element is more active after ultrahigh pressure treatment, thus rapidly be oxidized in the air and forms an oxide film on metal surface.

A distinct dual-phase structure of α-Mg and β-Li is detected in the as-cast alloys, as evidenced by optical microscopic images (**Fig. 1b-e)**, wherein α-Mg phase and β-Li phase appear as light and dark colors, respectively. The α-Mg phase in the Mg-8Li-AC alloy presents a typical dendrite structure, but it changes into a rod-like form after adding Y element. Theoretically, the melting point of metals increases with the increment of externally applied pressure. According to our previous experiments [16], the melting point of Mg alloys varies into about 1000-1100ºC at 6 GPa. In this regard, the samples mainly occurred ultrahigh solution heat treatment at 6 GPa and 700 °C. As shown in **Fig. 1c**, the distribution of α-Mg and β-Li in Mg-8Li-UHP-700 is more homogenous than those in Mg-8Li-AC, whereas there is still an obvious dual-phase structure in terms of XRD test results. In contrast, the microstructure of Mg-8Li-Y-UHP-700 is more uniform without apparent dual-phase structure. The course phases varied to fine dispersed particles in the grain or along the grain boundary on the surface of Mg-8Li-Y-UHP-700.

The high-resolution microstructures of Mg-8Li-1Y-AC and Mg-8Li-Y-UHP-700 alloys were further investigated by scanning electron microscopy (SEM), and the content of each element in the alloys was detected by energy dispersive spectrometer (EDS). As shown in **Fig. 2a**-**b** and **d**-**e**, some cuboid particles of second phase are observed on the surface of both alloys, which are identified as Y-rich phase according to EDS analysis (**Fig. 2c**). Noticeably, Li is too light to be detected in the EDS. Moreover, the size of Y-rich phase particles on Mg-8Li-Y-UHP-700 is smaller with a size range of 300-800 nm (**Fig. 2e**), and more evenly distributed compared with Mg-8Li-Y-AC, implying that the ultrahigh pressure condition inhibit the growth of Y-rich particles.

3.2. Corrosion properties

Fig. 3 shows the electrochemical results of samples, in relative to OCP,

polarization curves, electrochemical impedance spectrums and corrosion rate by weight loss. The OCP curves record the potential change of the alloy after soaking in 3.5 wt.% NaCl solution for 5 h (**Fig. 3a)**, where according to the variation of OCP, the electrode potential on the alloy surface tends to be stable after moving in the positive direction due to the gradual formation of corrosion products. The great fluctuation of the OCP in Mg-8Li-AC and Mg-8Li-UHP-700 indicates that the oxide film formed on the alloy surface is unstable. As for the OCP value of Mg-8Li-Y-AC, it initially increases, and then suddenly decreases after about 25 min, indicating that the alloy surface film breaks [18]. Noticeably, the potential of Mg-8Li-Y-UHP-700 decreases at the initial stage of immersion, then it gradually increases after ~15 min, and finally stabilizes.

Fig. 3b shows the polarization curves of the alloys, where the anode and cathode branches are asymmetrical. The cathodic polarization curves of Mg-8Li-AC, Mg-8Li-UHP-700, Mg-8Li-Y-AC and Mg-8Li-Y-UHP-700 are similar, corresponding to water reduction process. The anode curves of Mg-8Li-AC and Mg-8Li-Y-AC show a sharp increase of the current density once the applied potential exceeds corrosion potential. However, both Mg-8Li-UHP-700 and Mg-8Li-Y-UHP-700 exhibit a transition potential on the anode polarization curves or membrane breakdown potential (P_{men}). When the electric potential is less than the breakdown potential, the dissolution of the alloy is inhibited [19]. Compared with Mg-8Li-UHP-700 (-1.59V), the P_{men} of Mg-8Li-Y-UHP-700 is more positive (-1.48V), representing that the oxide film on the surface of the alloy has a good protective effect. On the other hand, the cathode branches are used to estimate the corrosion current density (I_{corr}). The I_{corr} values of Mg-8Li-AC, Mg-8Li-UHP-700, Mg-8Li-Y-AC and Mg-8Li-Y-UHP-700 are 1.24×10^{-4}, 3.42×10^{-5}, 1.08×10^{-4}, and 1.01×10^{-5} A/cm^2, respectively. The corrosion rate of weight loss **(Fig. 3c)** shows that the corrosion rate of Mg-8Li-AC is ~191.93 mm/y, which is a considerably higher than that of other samples. Conversely, the Mg-8Li-Y-UHP-700 has the lowest corrosion rate (~0.47 mm/y), which is close to high purity magnesium (~0.38 mm/y).

Nyquist diagrams (**Fig. 3d**) exhibit that Mg-8Li-AC, Mg-8Li-UHP-700 and Mg-8Li-Y-AC are mainly composed of a capacitive ring and an inductive ring, while Mg-

8Li-Y-UHP-700 consists of two capacitive rings. The high frequency capacitor loop may relate to the charge transfer resistance of the alloys, in which the medium and low frequency capacitance loop corresponds to the resistance of the surface film, and the low frequency inductance loop reflects to the adsorption of corrosion products [20]. Theoretically, alloys with larger capacitive loop radii exhibit lower corrosion rates and better corrosion resistance. The order of capacitor circuit diameters is Mg-8Li-Y-UHP-700 > Mg-8Li-UHP-700 > Mg-8Li-Y-AC > Mg-8Li-AC, indicating that Mg-8Li-Y-UHP-700 has the best corrosion resistance. Equivalent circuit **(Fig. 3e-f)** mainly includes solution resistance (R_s), charge transfer resistance (R_{ct}), double layer (Q_{dl}) at metal/electrolyte interface, film resistance (R_f) and film capacitor (Q_f), and inductive resistance (R_L) and inductive reactance (L). **Table 1** shows the summary of the fitting results of Nyquist diagram. The charge transfer resistance of Mg-8Li-AC, Mg-8Li-UHP-700 and Mg-8Li-Y-AC decreases gradually with the increasing time, indicating that the corrosion rate of the alloys rises progressively. In contrast, the R_{ct} of Mg-8Li-Y-UHP-700 increases with extending soaking time, and reaches ~1771.6 ohm·cm^2 after 12 h, revealing that the surface film of the alloy can effectively prevent the penetration of electrolytes.

To explore the corrosion resistance of the film on the alloy surface, the corrosion morphologies and corrosion substrates were analyzed (**Fig. 4**). As shown in **Fig. 4a**, **4c**, and **4e**, the surfaces of Mg-8Li-AC, Mg-8Li-UHP-700 and Mg-8Li-Y-AC are uneven, and a large number of corrosion products accumulate on whole alloy surface. The corrosion products are loosely attached to the matrix and continuously peel off during immersion. As indicated in **Fig. 4b**, **4d**, and **4f**, the corroded substrates of Mg-8Li-AC, Mg-8Li-UHP-700 and Mg-8Li-Y-AC are extremely rough with a great of protrusions and pits after removing corrosion products. In contrast, the surface of Mg-8Li-Y-UHP-700 is relatively flat, and the corrosion products are evenly distributed on the surface without obvious local corrosion (**Fig. 4g**). The corrosion substrate of Mg-8Li-Y-UHP-700 is uniform due to moderately flat with small corrosion pits (**Fig. 4h**). Undoubtedly, the dense corrosion product film on the surface of Mg-8Li-Y-UHP-700 provides effective protection. The composition of corrosion products was identified by XRD (**Fig.**

4i). Diffraction peaks of $Mg(OH)_2$ are detected on all alloys after soaking in 3.5 wt.% NaCl solution for 12 h. The incomplete corrosion phase (Y_2O_3) of Mg-8Li-Y-AC and Mg-8Li-Y-UHP-700 is also detected implying that Y_2O_3 does not participate in the corrosion process, which maybe enhances the density of the corrosion product film [21]. Meanwhile, the diffraction peak of Li_2CO_3 is detected only in Mg-8Li-Y-UHP-700.

3.3 *In-situ* corrosion characters

To clarify macroscopic evolution of surface films, the alloys were *in-situ* recorded by high definition CCD video microscope (**Movie 1**). As shown in **Fig. 5**, differing from Mg-8Li-AC, Mg-8Li-UHP-700 and Mg-8Li-Y-AC, a clear and intact surface area is observed in Mg-8Li-Y-UHP-700, without apparent local corrosion but color changes remarkably. Specifically, three distinct characters are observed during the *in-situ* immersion process of Mg-8Li-Y-UHP-700. The first character is a rapid dissolution/formation process of a black oxide film. The alloy surface is oxidized to break after 7 h. Then, the black oxide film, confirmed to be Li_2CO_3 by XRD results, forms on the alloy surface and quickly covers the entire metal surface (**Fig. 6a-c**). It persists for ~15 min, and finally dissolves (**Fig. 6d-e**). Some layered patterns are observed on the metal surface. It is worthy to note that this process occurred again and again, revealing that Li_2CO_3 remains a dynamic dissolution/formation equilibrium during the corrosion process (**Movie 2**). Additionally, this dynamic dissolution/formation equilibrium process has also confirmed by near *in-situ* XRD tests (**Fig. 6f-g**). The intensity of diffraction peaks for each phase is higher at the early stage of soaking. The intensity of each diffraction peak decreases to different degrees as soaking. The diffraction peak intensity of Li_2CO_3 decreases obviously after immersion for 3.5 h, but gradually increases after 8 h, and then the diffraction peak intensity of Li_2CO_3 rises again after 12 h. The intensity change contour line corresponding to the XRD pattern is shown in **Fig. 6g**, and the intensity change is consistent with the described process. It indicates that Li_2CO_3 can be quickly dissolves and generates in the electrolyte solution.

The second character is the self-healing process of oxide film (**Fig. 7a-e， Movie 3**). The alloy was took out after immersing in NaCl solution for 44 h, rinsed to dryness

with clean water, and then immersed again in NaCl solution. The alloy surface has no change at the initial immersing stage, some cracks appear on the alloy surface in the middle stage (**Fig. 7b-d**), and the cracks disappear in the later stage (**Fig. 7e**). During this period, the appearance of cracks is accompanied by the presence of the black oxide film. The results show that the Li_2CO_3 film can self-repair and fill the cracks in time to ensure the integrity and density of the oxide film.

The third character is the stable accumulation of corrosion products on the surface (**Fig. 7f-j, Movie 4**). To verify the changes of the surface film during the long-term soaking process, the samples were immersed in NaCl solution for ~250 h. The interval appearance between white corrosion products of $Mg(OH)_2$ and black Li_2CO_3 are observed on the surface of Mg-8Li-Y-UHP-700 with increasing immersion. Simultaneously, the alloy section was observed to estimate the thickness of the surface film on Mg-8Li-Y-UHP-700 for different soaking times (**Fig. 8**). It clearly shows the variation of the corrosion product film thickness on Mg-8Li-Y-UHP-700 after immersion in 3.5 wt.% NaCl solution for 1, 3, 5 and 7 days. When it is over 7 days, the thickness of composite oxide film remains relatively stable.

3.4 Corrosion mechanism

The outstanding corrosion resistance of Mg-8Li-Y-UHP-700 alloy is chiefly related to unique oxide film. Firstly, the compact structure of oxide film plays an important role in preventing the contact between the solution and alloy. The Pilling-Bedworth ratio (PBR) represents the ratio of the volume of formed oxide or any other compound to the volume of metal consumed to form metal oxides, which is an important parameter to evaluate the protection performance of oxide films against the matrix metal [22]. The calculation formula is as follows:

$$PBR = V_{oxide} / V_{alloy} = M_{oxide} \times \rho_{alloy} / (n \times \rho_{oxide} \times M_{alloy}) \quad (1)$$

where V_{oxide} is the volume of generated oxide, V_{alloy} is the volume of metal consumed to form an oxide, M_{oxide} is the molar mass of the formed oxide, ρ_{alloy} is metal density, n is the number of metal atoms per molecule of oxide, M_{alloy} is the atomic mass of a metal and ρ_{oxide} is the density of the formed oxide. The PBR values of Li_2CO_3, Y_2O_3, MgO and $Mg(OH)_2$ are approximately 1.30, 1.66, 0.83, and 1.82, respectively. Basically,

when PBR < 1, the oxide film has a low rate of coverage on the alloy surface and the protection performance is comparatively poor. When PBR > 3, the oxide film is easy to crack and fall off due to compressive stress. Therefore, the formation of a dense oxide film requires a PBR value between 1 and 2 [23]. The PBR (0.83) of MgO is lower than 1.0, indicating that the MgO film cannot inhibit further oxidation. The PBR value of $Mg(OH)_2$ is 1.82, between 1 and 2. Nevertheless, the $Mg(OH)_2$ film has a weak protective effect on the alloy due to the loose and porous nature of the $Mg(OH)_2$ film and its easy conversion into $MgCl_2$ in Cl^--containing solutions [24]. The PBR values of Li_2CO_3 and Y_2O_3 are both between 1 and 2. Therefore, the composite containing $Mg(OH)_2$, Li_2CO_3 and Y_2O_3 provide prerequisites to form stable and dense protective films.

Secondly, dynamic dissolution/regeneration of rich Li_2CO_3 film can fill the crack in $Mg(OH)_2$ film, effectively eliminating the shortage of common oxide film. Hue-Saturation-Intensity (Lightness) (HSI or HSL) color model has been performed to investigate this role. The HSI color model, proposed by H.A.Munseu in 1915, reflects the way that the human visual system perceives color through three basic characteristic quantities (i.e. hue, saturation and intensity) [25]. Hue (H) can describes a solid color and is defined as the wavelength of the color. Saturation (S) is a measure of the degree to which a solid color is diluted by white light and represents the depth of the color. Lightness (L) is a subjective description and embodies the colorless concept. Intensity (gray level) is the most useful descriptor of a monochrome image, which is measurable and easy to interpret. The HSI model has become a good tool for color description based image processing methods, making them natural and intuitive [26]. The HIS value of the surface color on Mg-8Li-Y-UHP-700 in the *in-situ* immersion video was measured by Take Color picker software. As shown in **Fig. 9a**, the alloy surface is bright and the corresponding brightness is extremely high before immersion. The alloy surface color becomes darker over time. The corresponding intensity of the alloy will first decrease and then increase due to the formation and dissolution of black Li_2CO_3 film. The statistical results are consistent with the test results, indicating that Li_2CO_3 can be quickly dissolved and generated in the electrolyte solution. The occurrence time and

duration of some black Li_2CO_3 oxide films is shown in **Fig. 9b**. The appearance time of the black Li_2CO_3 film is about 7, 19, 44, 57, 71 and 85 h, and the corresponding duration is around 0.27, 0.45, 0.78, 0.92, 1.14 and 1.32 h, respectively. The time span of Li_2CO_3 appearance is large in the early soaking stage, while the interval of Li_2CO_3 appearance is relatively stable in the middle stage of soaking, ranging from 13 to 14 h. This increasing duration of the Li_2CO_3 film demonstrates that the dynamic dissolution/formation equilibrium time of Li_2CO_3 is growing.

Finally, the self-repair character of composite oxide film attribute to good anti-corrosion properties of Mg-8Li-Y-UHP-700 alloy. As shown in **Fig. 9c**, the crack occurrence time and self-repair time of were calculated. The repair time of surface cracks increases with immersing, which is consistent with the increased dynamic formation/dissolution equilibrium time. **Fig. 9d** shows the thickness variation of corrosion product layers under different soaking time (corresponding to **Fig. 8**). Obviously, the thickness of the corrosion product layer increases with time, and the generation rate is faster in the initial stage but slower in the later stage, increasing the efficiency of composite film. In addition, the formation of Li_2CO_3 instead of Mg based compound remarkably reduces hydrogen content, increasing the integrity of oxide film. The large amount of H_2 gas is produced on surface film during the formation of Mg compounds. Conversely, the existence of Li_2CO_3 makes up for the loose defect of flaky $Mg(OH)_2$, enabling the oxide film to provide long-term protection [19].

As comprehensively analyzed above, the possible corrosion mechanism has been illustrated in **Fig. 10**. Mg-8Li-Y becomes more active after ultrahigh pressure and heat treatment. When the alloy is exposed to the atmosphere, Li element is oxidized rapidly, forming a layer of Li_2CO_3 oxide film on the metal surface. When the sample is immersed in NaCl solution, partial Li_2CO_3 dissolves due to its large solubility constant. Meanwhile, the alloy is eroded by Cl^- to form $Mg(OH)_2$. $Mg(OH)_2$ accumulates on the metal surface as time goes on. The cracking of the surface film appeared due to the loose and porous $Mg(OH)_2$ film and the produced H_2. Simultaneously, the lithium in the alloy and/or the dissolved lithium ions combine with the carbon dioxide in the electrolyte solution, resulting in continuous and rapid generation of Li_2CO_3. This

regenerative Li_2CO_3 fills the cracks of surface film until completely repaired, accounting for outstanding corrosion resistance.

4 Conclusions

Mg-8Li-AC, Mg-8Li-UHP-700, Mg-8Li-Y-AC and Mg-8Li-Y-UHP-700 alloys have been investigated by electrochemical measures and *in-situ* immersion tests, and the obtained Mg-8Li-Y-UHP-700 has the excellent corrosion resistance. The microstructure, corrosion properties and anti-corrosion mechanisms of the alloys are discussed. The main conclusions are summarized as follows:

- Mg-8Li-AC, Mg-8Li-UHP-700, Mg-8Li-Y-AC and Mg-8Li-Y-UHP-700 have the typical dual-phase structures of α-Mg and β-Li. Mg-8Li-Y-AC and Mg-8Li-Y-UHP-700 have the Y-rich phase in addition to α-Mg and β-Li phases. Moreover, the dimension of Y-rich particles is greatly reduced after ultrahigh pressure treatment.
- The corrosion rate of Mg-8Li-Y-UHP-700 is only ~0.47 mm/y after immersed in 3.5 wt. % NaCl solution for 200 h, which is better than the majority of Mg alloy reported so far. A quite flat corroded surface means a uniform corrosion occurs on alloy surface.
- Dependent on *in-situ* observation and near *in-situ* production identifications, the outstanding corrosion resistance of Mg-8Li-Y-UHP-700 stems from three aspects: compact composite oxide film, dynamic dissolution/regeneration of Li_2CO_3-rich phase, and self-repair character of composite film. Namely, when cracks appear on the alloy surface film, the regenerative Li_2CO_3 rapidly fills the cracks of surface film until completely repaired, resulting in good corrosion resistance.

Acknowledgement

We greatly acknowledge the financial support from National Natural Science Foundation of China (52171126, 51971194), the Natural Science Foundation of Hebei Province for Innovation Groups Program (No. 2022203003), and Ministry of Education Yangtze River Scholar Professor Program of China (No. T2020124). We would like to express our gratitude to Scientific research start-up fund for high-level talents of Yanshan University of China (No. 8190492).

Reference

[1] A. Dobkowska, B. Adamczyk – Cieślak, M. Koralnik, W. Chromiński, J. Kubasek, J. Ciftci, D. Kuc, J. Mizera, Corrosion behavior of fine-grained Mg-7.5Li-3Al-1Zn fabricated by extrusion with a forward-backward rotating die, J. Magnes. Alloy., 10(2022) 811-820.

[2] A. Dobkowska, B. Adamczyk – Cieślak, J. Kubásek, D. Vojtěch, D. Kuc, E. Hadasik, J. Mizera, Microstructure and corrosion resistance of a duplex structured Mg-7.5Li-3Al-1Zn, J. Magnes. Alloy., 9(2021) 467-477.

[3] C.Q. Li, X. Liu, L.J. Dong, B.Q. Shi, S. Tang, Y. Dong, Z.R. Zhang, Simultaneously improved mechanical strength and corrosion resistance of Mg-Li-Al alloy by solid solution treatment, Mater. Lett., 301(2021) 1-4.

[4] C. Li, B. Deng, L. Dong, B. Shi, Y. Dong, F. Peng, Z. Zhang, Effect of Zn addition on the corrosion behaviours of as-cast BCC Mg-11Li based alloys in NaCl solution, Mater. Design, 221(2022) 1-13.

[5] Y. Zou, S. Liu, Q. Wang, Y. Li, A comparative study on mechanical and corrosion behaviours of α/(α + β) Mg-Li alloys subjected to ultrasonic nanocrystal surface modification, Metals, 12(2022) 1-15.

[6] H. Li, C. Shao, D.F. Rojas, M. Ponga, J.D. Hogan, Micro-hardness and strain-rate-dependent compressive response of an ultra-light-weight Mg-Li-Al alloy, J. Alloy. Compd., 890(2022) 1-41.

[7] D.K. Xu, E.H. Han, Effect of quasicrystalline phase on improving the corrosion resistance of a duplex structured Mg–Li alloy, Scripta Mater., 71(2014) 21-24.

[8] Y.M. Yan, A. Maltseva, P. Zhou, X.J. Li, Z.R. Zeng, O. Gharbi, K. Ogle, M. La Haye, M. Vaudescal, M. Esmaily, N. Birbilis, P. Volovitch, On the in-situ aqueous stability of an Mg-Li-(Al-Y-Zr) alloy: Role of Li, Corros. Sci., 164(2020) 1-13.

[9] H. Yang, L. Wu, B. Jiang, W. Liu, J. Song, G. Huang, D. Zhang, F. Pan, Clarifying the roles of grain boundary and grain orientation on the corrosion and discharge processes of α-Mg based Mg-Li alloys for primary Mg-air batteries, J. Mater. Sci. Technol., 62(2021) 128-138.

[10] H. Ji, G. Wu, W. Liu, X. Zhang, L. Zhang, M. Wang, Origin of the age-hardening

and age-softening response in Mg-Li-Zn based alloys, Acta Mater., 226(2022) 1-15.
[11] G. Liu, W. Xie, G. Wei, Y. Yang, J. Liu, T. Xu, W. Xie, X. Peng, Dynamic recrystallization behavior and corrosion resistance of a dual-phase Mg-Li alloy, Materials, 11(2018) 1-11.
[12] L. Hou, M. Raveggi, X. Chen, W. Xu, K.J. Laws, Y. Wei, M. Ferry, N. Birbilis, Investigating the passivity and dissolution of a corrosion resistant Mg-33at.%Li alloy in aqueous chloride using online ICP-MS, J. Electrochem. Soc., 163(2016) 324-329.
[13] Y. Li, Z. Kang, X. Zhang, J. Pan, Y. Ren, G. Zhou, Fabricating an anti-corrosion carbonate coating on Mg Li alloy by low-temperature plasma, Surf. Coat. Tech., 439(2022) 1-8.
[14] W. Xu, N. Birbilis, G. Sha, Y. Wang, J.E. Daniels, Y. Xiao, M. Ferry, A high-specific-strength and corrosion-resistant magnesium alloy, Nat. Mater., 14(2015) 1229-1235.
[15] S. Zhang, Y. Sun, R. Wu, X. Wang, X.-B. Chen, C. Fernandez, Q. Peng, Coherent interface strengthening of ultrahigh pressure heat-treated Mg-Li-Y alloys, J. Mater. Sci. Technol., 51(2020) 79-83.
[16] H. Fu, B. Ge, Y. Xin, R. Wu, C. Fernandez, J. Huang, Q. Peng, Achieving high strength and ductility in magnesium alloys via densely hierarchical double contraction nanotwins, Nano Letters, 17(2017) 6117-6124.
[17] S. Tang, T. Xin, W. Xu, D. Miskovic, C. Li, N. Birbilis, M. Ferry, The composition-dependent oxidation film formation in Mg-Li-Al alloys, Corros. Sci., 187(2021) 1-8.
[18] L. Prince, X. Noirfalise, Y. Paint, M. Olivier, Corrosion mechanisms of AZ31 magnesium alloy: Importance of starting pH and its evolution, Mater. Corros., 73(2022) 1615-1630.
[19] J. Feng, H. Zhang, L. Zhang, G. Zou, J. Wang, Q. Peng, Microstructure and corrosion properties for ultrahigh-pressure Mg-Li alloys, Corros. Sci., 206(2022) 1-11.
[20] M.C. Delgado, F.R. García-Galvan, V. Barranco, S.F. Batlle: A measuring approach to assess the corrosion rate of magnesium alloys using electrochemical impedance spectroscopy. Magnesium Alloys, 2017. pp. 129-159.
[21] Q. Zhu, Y. Li, F. Cao, D. Qiu, Y. Yang, J. Wang, H. Zhang, T. Ying, W. Ding, X.

Zeng, Towards development of a high-strength stainless Mg alloy with Al-assisted growth of passive film, Nat. Commun., 13(2022) 1-8.

[22] Q. Jiang, D. Lu, C. Liu, N. Liu, B. Hou, The Pilling-Bedworth ratio of oxides formed from the precipitated phases in magnesium alloys, Front. Mater., 8(2021) 1-12.

[23] H. Cai, Q. Wang, Y. Zhao, J. Peng, N. Zhang, H. Wang, M. Suéry, J.J. Blandin, Influence of calcium on ignition-proof mechanism of AM50 magnesium alloy, J. Mater. Sci., 57(2022) 7719-7728.

[24] G. Williams, H.N. McMurray, R. Grace, Inhibition of magnesium localised corrosion in chloride containing electrolyte, Electrochim. Acta, 55(2010) 7824-7833.

[25] H. Zhao, Q. Li, H. Feng, Multi-focus color image fusion in the HSI space using the sum-modified-laplacian and a coarse edge map, Image Vision Comput., 26(2008) 1285-1295.

[26] W. Yin, X. Cheng, J. Xie, H. Cui, Y. Chen, High-speed 3D profilometry employing HSI color model for color surface with discontinuities, Opt. Laser Technol., 96(2017) 81-87.

Table 1 Fitting results of the EIS curves.

Samples	Time (h)	R_s (ohm cm^2)	Q_{dl} (F s^{n-1} cm^{-2})	R_{ct} (ohm cm^2)	L (H cm^{-2})	R_L (ohm cm^2)	Q_f (F s^{n-1} cm^{-2})	R_f (ohm cm^2)
Mg-8Li-AC	5	9.3	4.7×10^{-4}	15.7	103.1	2.3	--	--
	8	9.4	5.1×10^{-4}	8.8	24.2	2.2	--	--
	10	9.6	6.7×10^{-4}	5.7	18.1	2.0	--	--
	12	9.9	6.5×10^{-4}	4.3	9.81	1.8	--	--
Mg-8Li-UHP-700	5	9.6	2.4×10^{-4}	90.3	75.2	99.7	--	--
	8	9.2	1.9×10^{-4}	85.6	70.9	43.4	--	--
	10	9.2	2.8×10^{-4}	67.9	73.1	28.1	--	--
	12	9.7	2.2×10^{-4}	48.7	67.9	19.7	--	--
Mg-8Li-Y-AC	5	7.3	4.2×10^{-4}	33.2	51.3	13.3	--	--
	8	7.3	5.3×10^{-4}	32.3	10.1	12.6	--	--
	10	7.6	6.7×10^{-4}	28.4	7.7	9.2	--	--
	12	7.8	4.4×10^{-4}	26.6	1.9	4.2	--	--
	5	7.1	5.4×10^{-5}	1193.0	--	--	3.9×10^{-3}	360.1

Mg-8Li-Y-UHP-700	8	7.2	5.4×10^{-5}	1568.5	--	--	2.9×10^{-3}	569.3
	10	7.4	5.8×10^{-5}	1759.3	--	--	2.3×10^{-3}	849.9
	12	7.4	5.7×10^{-5}	1771.6	--	--	2.0×10^{-3}	1117.1

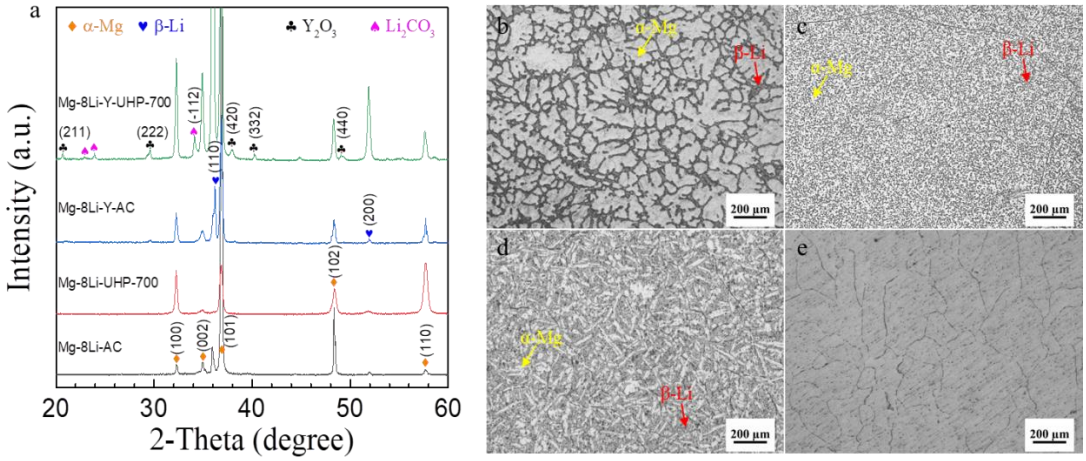

Fig. 1. (a) XRD patterns of four alloys. Optical micrograph images of (b) Mg-8Li-AC, (c) Mg-8Li-UHP-700, (d) Mg-8Li-Y-AC, (e) Mg-8Li-Y-UHP-700.

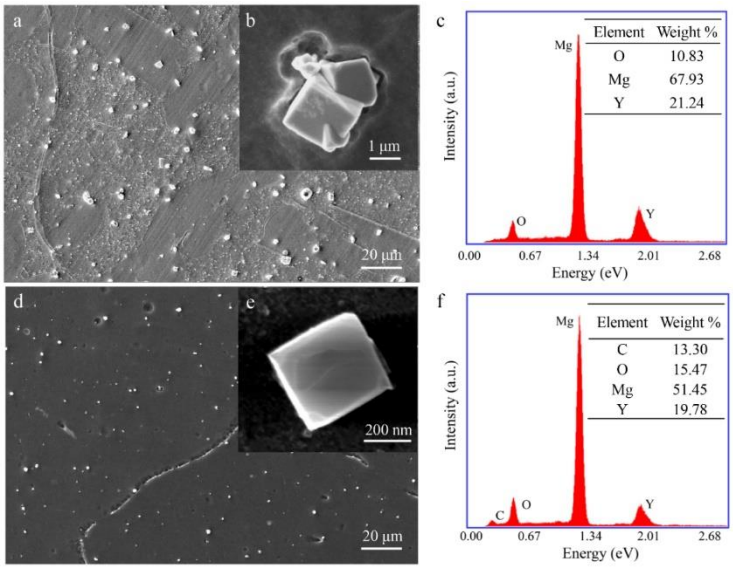

Fig. 2. SEM images and phase composition. (a) Low resolution and (b) high resolution of Mg-8Li-Y-AC, (c) corresponding EDS energy spectrum of the particle in (b); (d) low resolution and (e) high resolution of Mg-8Li-Y-UHP-700, (f) corresponding EDS energy spectrum of the particle in (e).

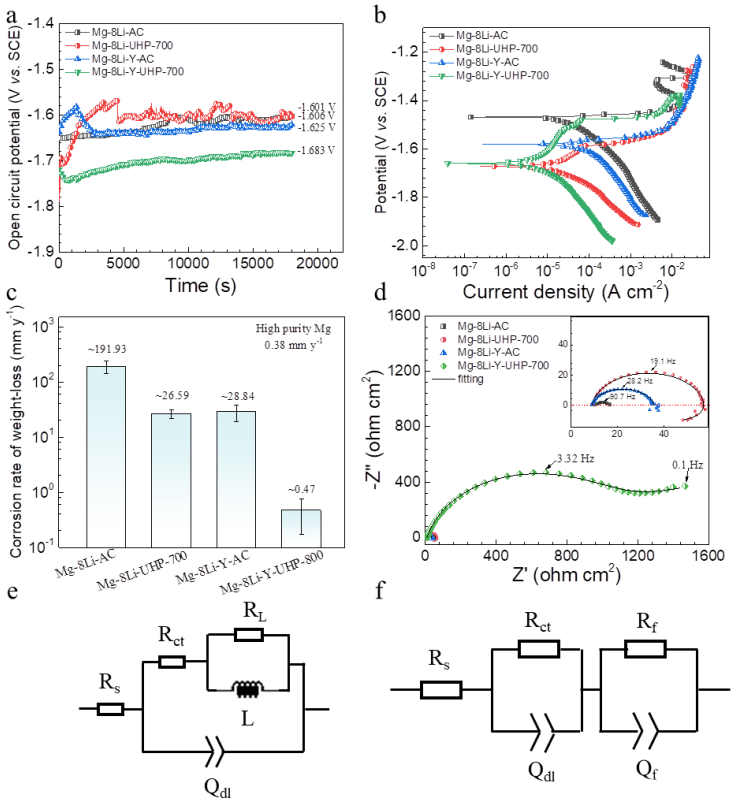

Fig. 3. Corrosion properties. (a) OCP curves. (b) Polarization curves. (c) The corrosion rate by weight loss. (d) Nyquist curves of EIS. (e) EIS fitting impedance and equivalent circuit for Mg-8Li-AC, Mg-8Li-UHP-700 and Mg-8Li-Y-AC. (f) EIS fitting impedance and equivalent circuit for Mg-8Li-Y-UHP-700.

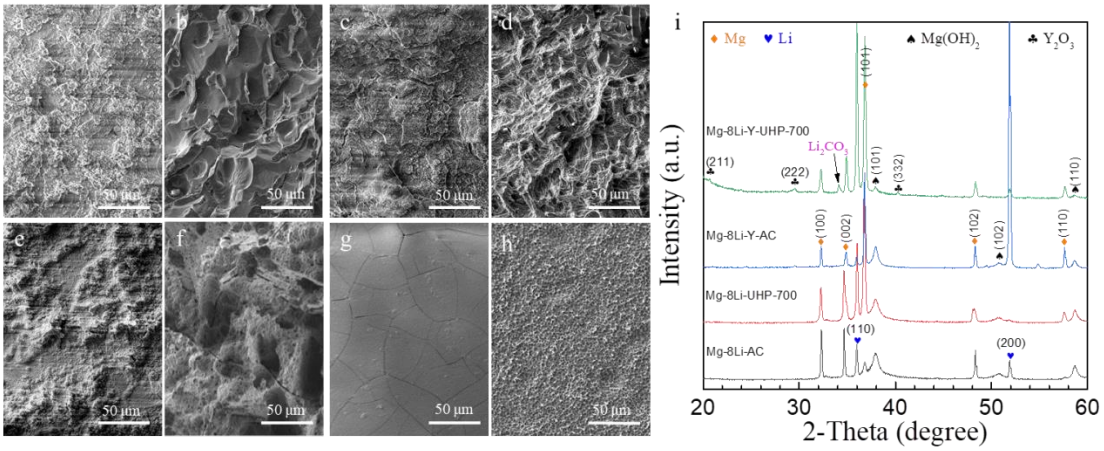

Fig. 4. Morphology variation of the alloys after immersed in 3.5 wt.% NaCl solution for 12 h and substrate morphology after removing the corrosion products: (a-b) Mg-

8Li-AC, (c-d) Mg-8Li-UHP-700, (e-f) Mg-8Li-Y-AC, (g-h) Mg-8Li-Y-UHP-700. (i) XRD spectrograms of the corrosion products after immersion in 3.5 wt.% NaCl solution for 12 h.

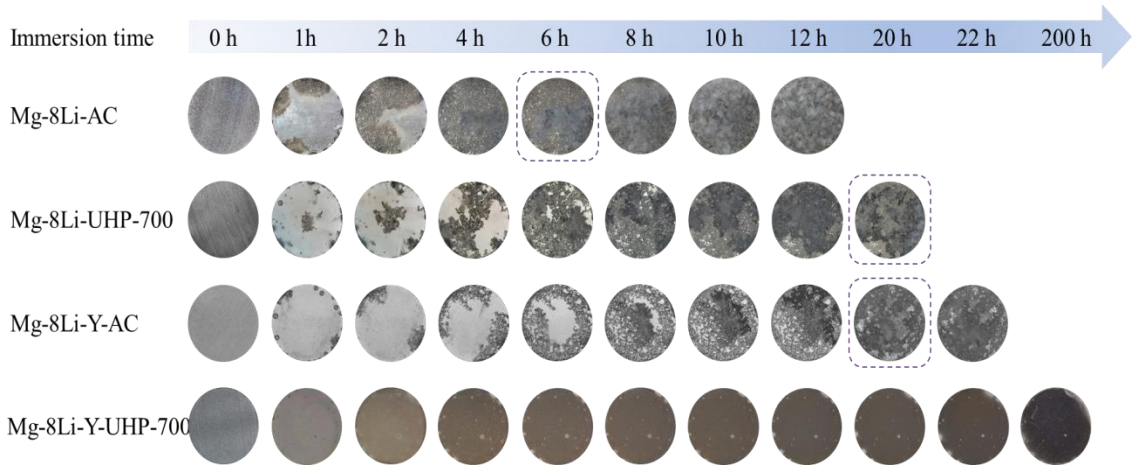

Fig. 5. *In-situ* macroscopic variations for the surface of alloys immersed in 3.5 wt.% NaCl solution. The actual diameter of the samples is 1 cm.

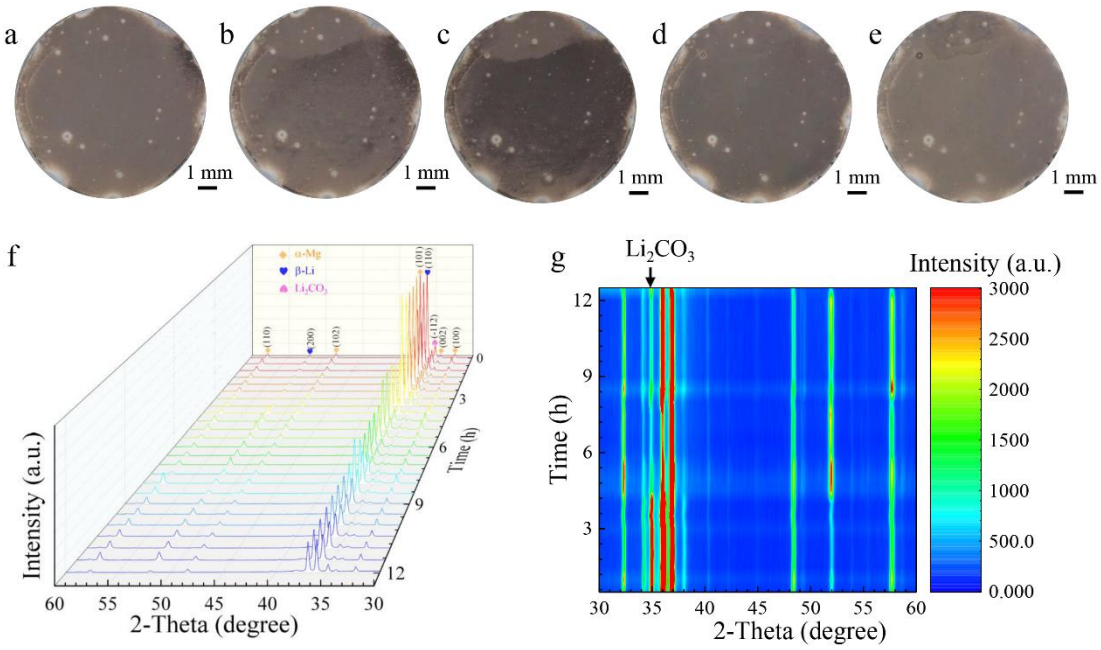

Fig. 6. Typical rapid formation/dissolution process of black oxide film. The relative time in this process: (a) 1 min, (b) 3 min, (c) 5 min, (d) 10 min, (e) 15 min. (f) Near-*in*-

situ XRD pattern of Mg-8Li-Y-UHP-700 after soaking in 3.5 wt.%NaCl solution for 12 h. (g) The contour of intensity variation corresponding to XRD patterns.

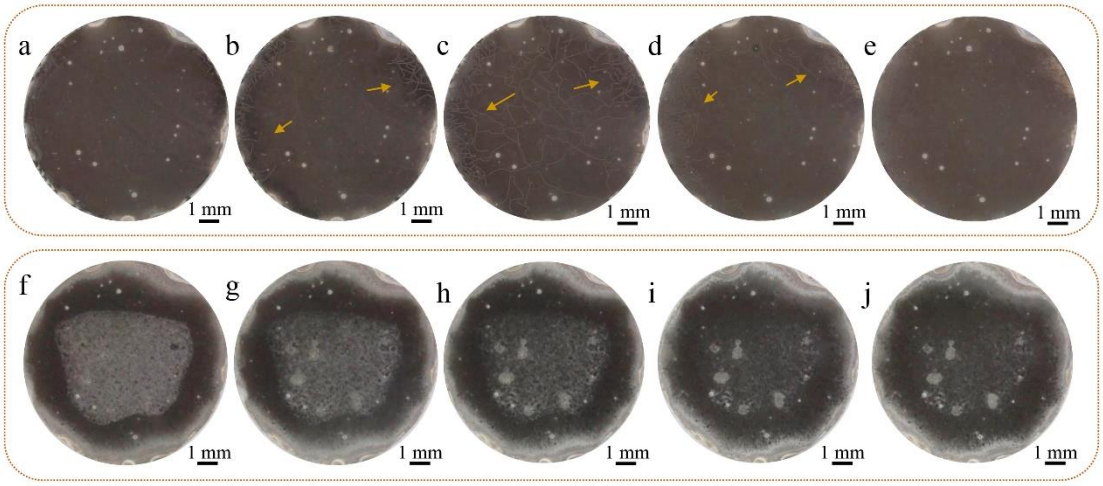

Fig. 7. Images of the self-healing process of the oxide film. The relative time in this process (a) 0 h, (b) 0.3 h, (c) 0.5 h, (d) 0.7 h, (e) 1.7. Images of the accumulation of corrosion products on the alloy surface. The relative time in this process (f) 0 h, (g) 3 h, (h) 6 h, (i) 9 h, (j) 12 h.

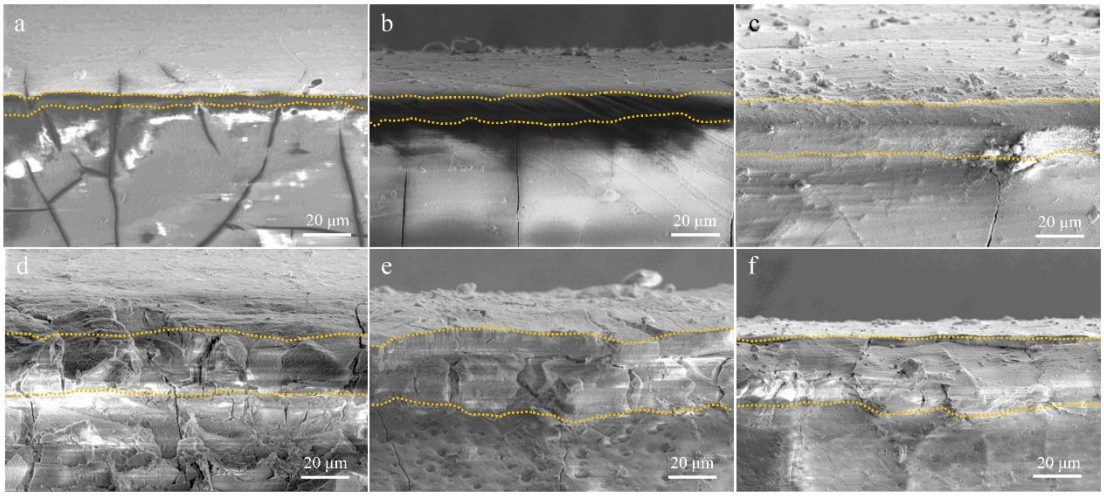

Fig. 8. Cross-section morphology images of Mg-8Li-Y-UHP-700 under different immersion time in 3.5 wt.% NaCl solution. (a) 1 d, (b) 3 d, (c) 5 d, (d) 7 d, (e) 9 d, (f) 11 d.

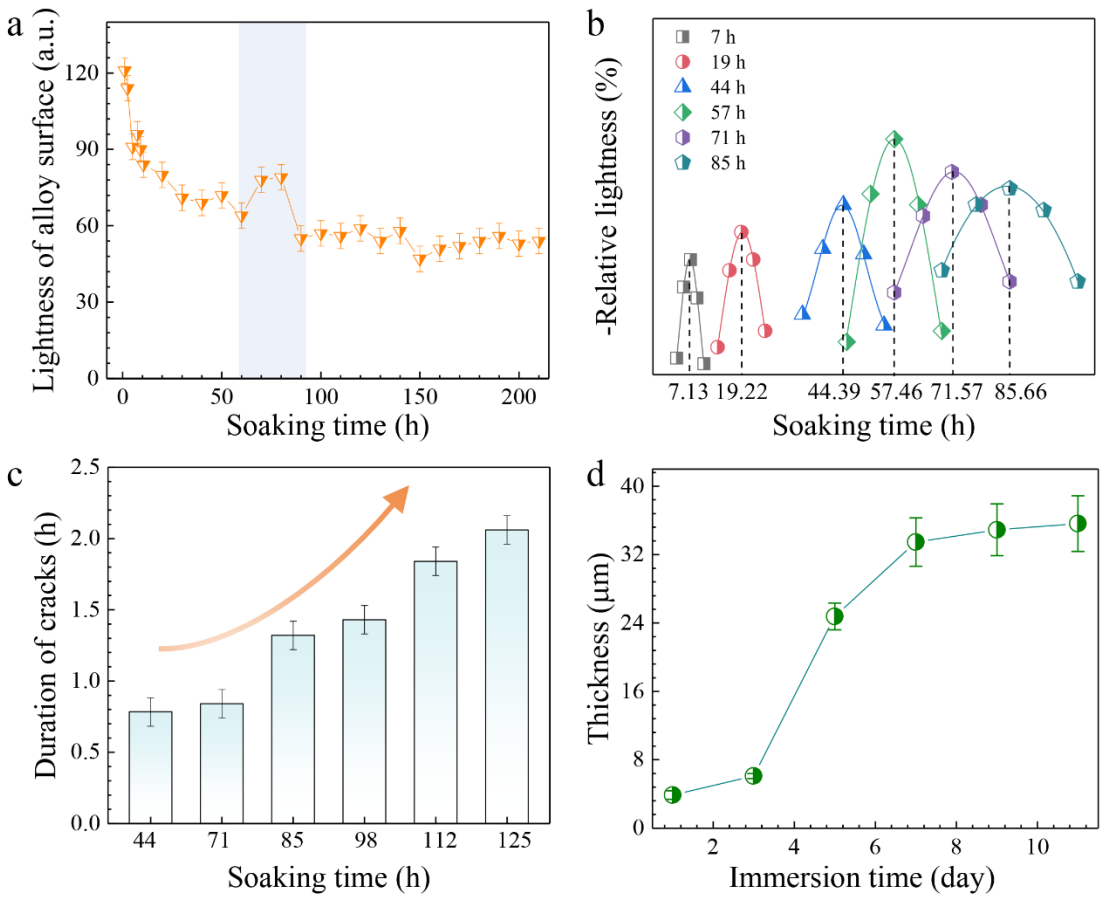

Fig. 9. *In-situ* immersion observation of Mg-8Li-Y-UHP-700. (a) The variation of alloy surface lightness. (b) The time interval for the formation of black lithium carbonate. (c) The self-repair duration after the appearance of cracks on the surface change. (d) The variation of corrosion product layer thickness over time.

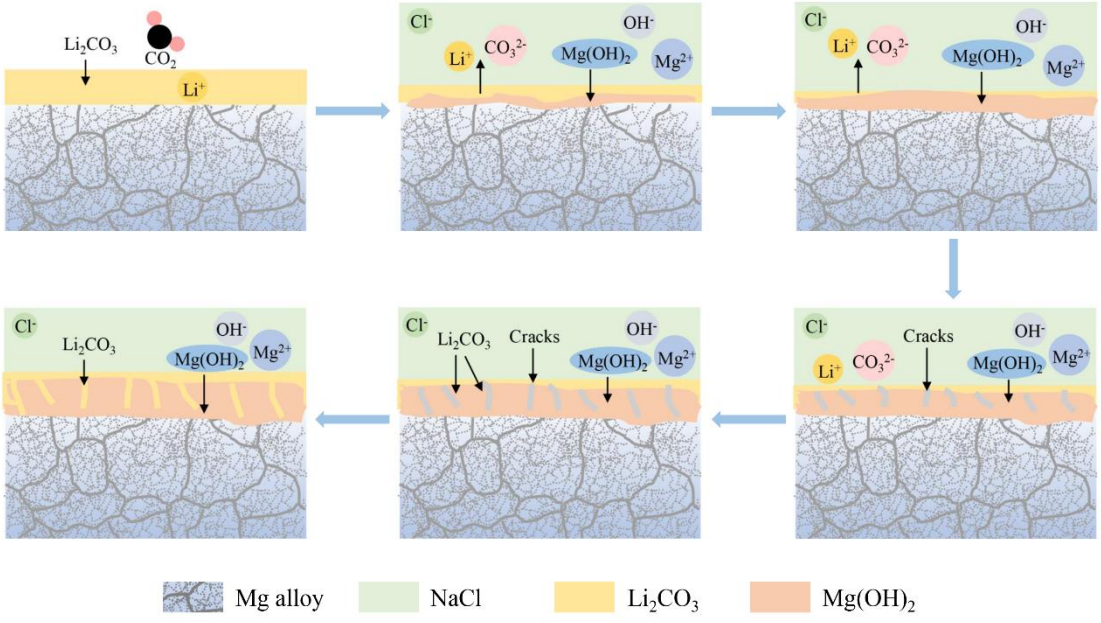

Fig. 10. Presentative schematic diagram of corrosion mechanism.

CRediT authorship contribution statement

Q.M. conceived the project. M.Y., J.F. and H.H carried out the syntheses and structural characterizations. T.N. and W.G. conducted the electrochemical reduction experiments. G.Z. and L.R. carried out the in-situ XRD experiment and provided the analyses. C.F. helped to write this manuscript. Q.M. was responsible for the overall direction of the project. All the other authors participated in preparing the manuscript and contributed to the discussion.